Gavin N. Nop, ⒾⒹ Durga Paudyal and ⒾⒹ Jonathan D. H. Smith

View Online   Export Citation

AVS Quantum Science

Ytterbium ion trap quantum computing: The current state-of-the-art

View Online   Export Citation   CrossMark

Gavin N. Nop,[1,2] Durga Paudyal,[1,3,a] (iD) and Jonathan D. H. Smith[1,2] (iD)

AFFILIATIONS

[1]Ames Laboratory, U.S. Department of Energy, Iowa State University, Ames, Iowa 50011, USA
[2]Department of Mathematics, Iowa State University, Ames, Iowa 50011, USA
[3]Electrical and Computer Engineering Department, Iowa State University, Ames, Iowa 50011, USA

[a]Author to whom correspondence should be addressed: durga@ameslab.gov

ABSTRACT

We present an overview of contemporary quantum computing with ytterbium ion traps, placing the emphasis on industry implementations. We provide brief, concrete descriptions of various key features, such as trap loading, electronic structure, qubit function, gates, error analysis, and benchmarking. We focus on the underlying science and current technologies to provide readers with a holistic picture of available techniques for using ytterbium in contemporary ion trap designs.

Published under an exclusive license by AIP Publishing. https://doi.org/10.1116/5.0065951

TABLE OF CONTENTS

I. INTRODUCTION

The history of classical computers is a progression from the first proofs of concept, using vacuum tubes, to the eventual sophistication of modern silicon-based architecture. Now, quantum computers are moving from proof of concept to practical design and are at the point of scaling to increasingly large numbers of coherent, well-connected qubits.

Ionic quantum computers have been strong contenders for the development of quantum computation since Cirac and Zoller demonstrated a feasible method of applying arbitrary unitary operations to

linear arrays of ions.[1] More recently, two industry quantum computers using ytterbium were introduced by Honeywell[2] and IonQ.[3] These computers take the valence electron in the outermost S shell of the ytterbium isotope ion ^{171}Yb$^+$ to encode the states of a qubit. There are two competitive architectures, namely, modular universal scalable ion-trap quantum computer (MUSIQC) and quantum charge-coupled device (QCCD).[4,5]

Why use a rare earth element at all? The [Xe] 4f^{14} 6s^1 electron configuration is attractive because of its hyperfine-to-optical coupling through the use of the P orbitals. In addition, it is reasonably simple to implement. Several elements and isotopes are potentially available for this configuration.

Why ^{171}Yb$^+$ specifically? The choice of this isotope was motivated by requiring nuclear spin 1/2, observational stability, and first-order Zeeman insensitive clock states. Radioactive isotopes might be considered, but the isotope must be stable and prevalent enough to be isolated from typical sources of the metal. Additionally, we require that ionization energies be reasonable and that ionized atoms be positively charged. ^{171}Yb$^+$ is the only isotope satisfying these constraints.

A. Outline

In this paper, we maintain a flexible structure for the benefit of a reader. We imagine the development of a quantum computer from scratch, following the design and execution to the final evaluation of the device.

We first consider the underlying physics involved in using ^{171}Yb$^+$ in a quantum computer, and then the architecture provided by the configuration of the ion trap.

With the basic blueprint in mind, the ensuing section considers details of the ion trap: 2D microfabrication, trap geometry, and topology for ion transport. Depending on the chosen configuration, this may be more or less trivial. However, critical initial decisions, such as magnetic field orientation and strength, will play into later design considerations.

Next, we consider the loading of ions into the ion trap. We briefly address the ionization process for ytterbium and similar atoms. Then, we consider the dual processes of ion initialization and readout. Thus, we can initialize a quantum computer and get readouts to determine coherence times.

We also examine ion transport, which is more relevant for the Honeywell design than the IonQ design. We give several ways that ions can be moved and manipulated, considering the implications for coherence. Additional complications arise when scaling up beyond simple linear ion trap designs.

Finally, we discuss qubit manipulation to implement gates. Since it is sufficient to implement all single qubit (SQ) gates together with a universal two qubit (TQ) gate, we first consider the more straightforward case of an SQ and then some possible TQ gates. This completes everything necessary to perform quantum computations. This paper then concludes with an analysis of error and performance.

We cover the MUSICQ (IonQ) and QCCD (Honeywell) architectures in parallel. To gain an understanding of either one, each section with its corresponding introduction should be read together with Subsections II A, III A, IV, V A, and VIII A.

The MUSIQC architecture used by IonQ and Sandia relies on a single chain of ions that share a motional bus, in some aspects similar to the original Cirac-Zoller proposal.[3,6] Ions are arranged in a string within a pseudo-potential well created by the trap. Initially, the ions

are loaded and cooled. They are then addressed by two lasers: a global beam addressing all the ions simultaneously and a local beam to address individual qubits.[3] Subsections IV B, VI A, and VIII B are specific to IonQ and Sandia.

The QCCD architecture uses an ion trap with sections of densely packed electrodes for the transport of individual ions. Once the ions are loaded, they are initially cooled. Then, they are manipulated into the desired configuration for a sequence of pulses to address them during gate implementation. Rearrangement and gate application repeat until the quantum program finishes. Advanced ion transportation is also possible in the MUSICQ architecture, although the IonQ computer does not use this during computation. The Honeywell device cools the ytterbium qubit during the run time via sympathetic cooling with barium without harming the qubit state.[7] Subsections III B, VI B, VI C, VI D, and VIII C are specific to Honeywell.

The error section offers a brief summary of widely used methods of performance assessment providing benchmarks for comparison between different quantum computers.

B. Standard notation

We establish standard notation for use throughout the paper. We refer to the elements ytterbium and barium as Yb and Ba in either their ionic or neutral states and, unless stated otherwise, these references default to ^{171}Yb$^+$ and ^{138}Ba$^+$, respectively.

For trap design, we assume a standard 3D right-handed xyz coordinate basis as in Fig. 1. We use x, y, and z as both variables and unit vectors interchangeably. Thus, the z-axis is used for axial motion, and the x-axis for transverse motion. The coordinate system is assumed to have its origin $(0, 0, 0)$ at the center of the linear array of ions. Due to the symmetry of the ion traps considered, this is well-defined for the x and z axes. For the y coordinate, we choose $y = 0$ to coincide with the position of the ions above the trap surface. In equations with variables which are not explicitly defined by the text (such as the first displayed equation in Sec. III), the variables are assumed to be tunable parameters with dimensions specified by the equation.
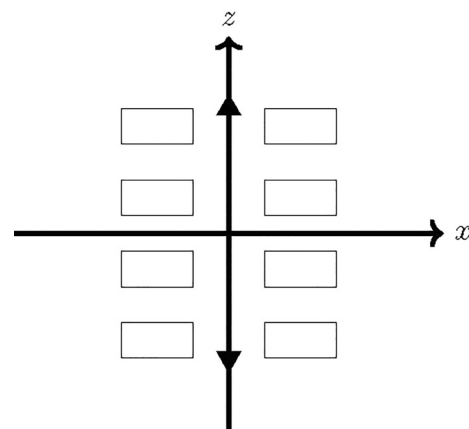

FIG. 1. A mockup of the standard coordinates used in the remainder of the paper. Here, the z-axis is the axis of freedom for ion transport, the x-axis is the transverse axis, uniquely defined by our assumption that all ion trap configurations are 2D, and the y-axis is perpendicular to the ion trap surface, with the positive direction pointing down away from the image.

In cases where we treat both motional states and electronic states, we use the notation $|n; e\rangle$, where n is the quantum number for the motional state and e determines the internal electronic state. The quantum numbers for the spin will be labeled as F, and the z-projection of spin is m_F. Due to the focus on ytterbium computers, $|0\rangle$ will refer to ${}^2S_{1/2}|F = 0, m_F = 0\rangle$ and the $|1\rangle$ state is embedded in the ${}^2S_{1/2}|F = 1, m_F = 0\rangle$ state. We use a one-dimensional quadratic approximation for the potential well containing the ions in the paper. Thus, the motional states are identified with the natural numbers as $n = 0, 1, \ldots$, and $\bar{n}$ refers to the average value of n over many trials. Since n is reserved for the motional states, we use the variable m to refer to the number of qubits in a quantum computer.

For all sections from IV A 2, we assume that each ion is cooled to the Lamb-Dicke regime, where changes of more than one in any motional quantum number are suppressed. For the precise mathematical definition, see Sec. IV A 2.

II. PRELIMINARIES ON YTTERBIUM

Ytterbium is a rare earth element, with atomic number 70, empirical radius 175 pm, weight 173.045 u, and first ionization energy 6.254 eV. The hyperfine gap has a 12.642 821 GHz qubit frequency,[9] and the first-order Zeeman insensitive clock states allow a magnetic field to quantify the electronic states, while minimizing the effect of a non-uniform magnetic field on the separation of the $|0\rangle$ and $|1\rangle$ states in different locations around the geometry of the ion trap.[8]

The ^{171}Yb$^+$ qubit was constructed using methods first implemented by Olmschenk et al.[8] The relevant large scale electronic structure is displayed in Fig. 2. The ${}^2S_{1/2}$ hyperfine levels encode the qubit states. Due to the electronic shielding provided by the surrounding $4f$ states, these hyperfine levels are insensitive to first order changes in magnetic fields.

In Fig. 2, we visualize the full hyperfine structure of the relevant states in the case of ^{171}Yb$^+$, which has a nuclear spin of 1/2, leading to well-defined hyperfine splitting. As noted earlier, the $|0\rangle$ state is embedded in the ground state of the ion, while the $|1\rangle$ state is embedded in the ${}^2S_{1/2}|F = 1, m_F = 0\rangle$ state. A homogeneous magnetic field
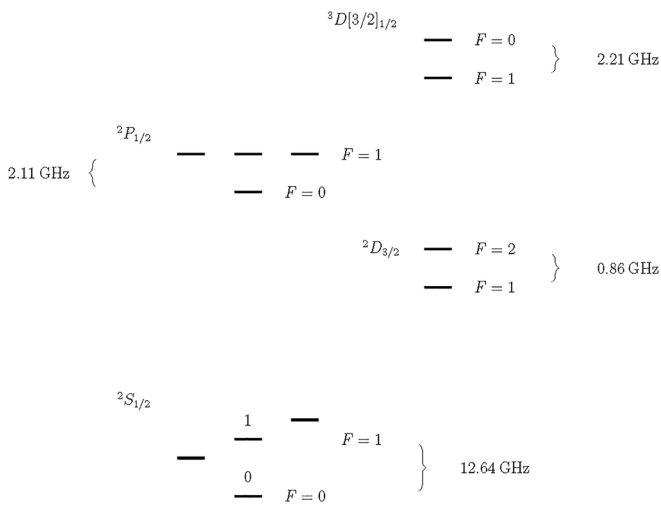

FIG. 2. ^{171}Yb$^+$ electronic structure. The $4f$ orbitals provide spherical insulation of inner shells acting as a buffer against external electronic fields.

of 5 G $\pm 2 \times 10^{-1}$ mG applied in the $x + z$ direction to the trap in the Honeywell machine implements a quantization axis.[7] Similarly, IonQ maintains a magnetic field of 5.2 G $\pm 2 \times 10^{-1}$ mG.[9] The magnetic variation here refers to the spatial variation over the length of the trap. Using a Helmholtz coil, which has $\frac{d^2B}{dz^2} = 0$ at the center, allows for the refined spatial control needed to ensure variations in the magnetic field that are small enough not to interfere with operations on qubits.

A. Selection and loading

To load ions into the ion trap, a loading slot or vertical laser access can be added, avoiding the possibility of contaminating the electrode surfaces used to control the ions. A common method of loading is photoionization, which allows the selection of ^{171}Yb$^+$ during ionization. If, after loading and testing, any ions are found not to be of the appropriate isotope, they are ejected, and a renewed attempt at loading is made.

In one possible choice of wavelengths for the photo-ionization of ^{171}Yb$^+$, two dichroic beams, tuned to 369.53 and 398.91 nm, illuminate a neutral Yb atom emitted from a heated Yb metal. The 398.91 nm light is tuned to the $S_{1/2} \leftrightarrow P_{1/2}$ transition, which is ion-specific, allowing the selection of the ^{171}Yb neutral atoms, and the 369.53 nm wavelength ionizes the Yb atom, as shown in Fig. 3. (As noted in the Appendix, a similar approach was used for the barium in the Honeywell computer.)

III. ION TRAP DESIGN AND INITIAL CONSIDERATIONS

We examine two primary aspects of ion trap design, namely, the static configuration and ion locomotion. The IonQ devices serve as examples for the first aspect. The second aspect involves a linear Paul trap with a more advanced electrode configuration, allowing the rearrangement of ions in the gate through combination, separation, swapping, and locomotion. The Honeywell device serves as our example here.

3D Paul traps are relatively easy to fabricate. However, 2D microfabrication allows for a tighter specification on the construction of the trap. Additionally, the convenient location of the electrodes allows for direct access to the ions by lasers above the surface with fewer concerns about arranging beams to avoid interference with the electric components. Furthermore, the 2D design allows for accurate manufacturing with the reduced use of the necessary conventional materials and with less electric field noise near the surfaces of the electrodes, thus maintaining more faithful qubit states.

We will be considering linear Paul traps and will spend most of our time focusing on the control of ions in the xy-plane at the center of the trap with the radio frequency (RF) electrodes and the control electrodes lining the trap for fine-grained control. The ions may be trapped along the z-axis with the use of simple DC voltages. We take V_0 to represent the absolute time-average of the potential, and Ω as the radial frequency of the trap. In the xy-plane, the time-dependent potential of the basic Paul trap is written as

$$V(x, y, t) = \frac{V_0}{2}\left(1 + \frac{x^2 - y^2}{R^2}\right)\cos \Omega t$$

(using our convention for the tunable length scale parameter R). Earnshaw's theorem states that a collection of point charges cannot be held in a static equilibrium by electrostatic charges. To circumvent
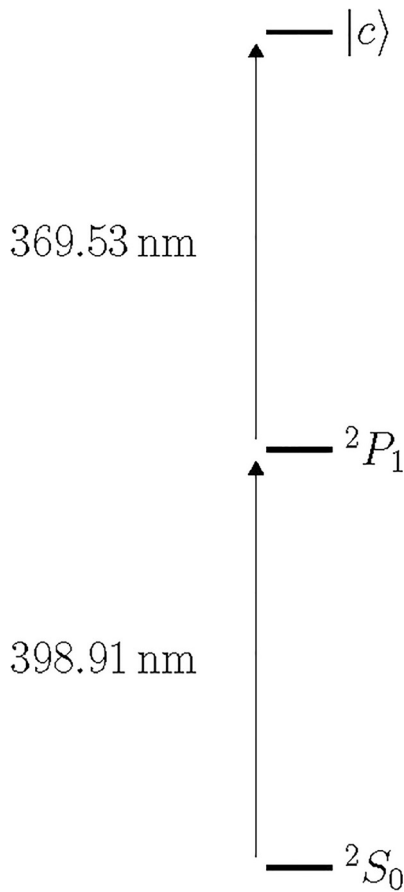
Fig. 3. Sample transitions used in the photoionization of the desired ytterbium isotope. Two beams of light, each corresponding to one of the transition frequencies, illuminate a thermal stream of ions. Tuning guarantees that only $^{171}Yb^+$ is ionized and then captured in the ion trap.

this, the ions are centered and trapped at the saddle point of an oscillating pseudo-potential.[10]

In essence, a linear Paul trap is similar to a quadrupolar mass filter with two electric fields at both ends capping the trap. In a linear trap, the radial frequency ω_x must be made high enough relative to the axial frequency ω_z in order to keep the ions aligned with the z-axis of the trap.

The Mathieu equation $\ddot{u} + [a + 2q\cos\Omega t]\frac{\Omega^2}{4}u = 0$ describes the motion of the ions. Here, u is the ion position. The path of an ion can be found by considering the force $F = m\ddot{u}$. Different ionic masses lead to different stable zones, parametrized by the dimensionless constants q and a. The equation can be solved explicitly in simple cases. For instance, in the case where $|q|, |a| \ll 1$, the first-order solution for the ion is $u(t) \sim A\cos{(\omega_i + \phi)}[1 + \frac{q}{2}\cos\Omega t]$, where $\omega \sim \frac{1}{2}\sqrt{a + q^2/2}$, A is the amplitude and ϕ is a phase factor dependent on initial conditions. In more complex cases, the numerical calculation or Monte Carlo methods can be used to fine tune the correct constants.

The motion of ions in a Paul trap is split into two types. The first is the secular motion. This is the motion that results from the movement of the ion, treating the containing pseudo-potential as a quadratic well. In the above solution, this corresponds to the frequency ω and amplitude A. The second type is the motion corresponding to the $\cos\Omega t$ term, the motion resulting directly from the oscillating potential, which we refer to as micromotional.[11]

A. 2D Paul trap

In the forthcoming discussion of microfabricated ion traps, we note that a simple static voltage applied to electrodes at the ends of the traps is sufficient to keep the ions trapped in the z axis. As this is used in conjunction with the oscillating quadrupolar radial confinement field, it does not violate Earnshaw's theorem. For that reason, we treat the axial containment separately and focus on the transverse containment first.

When considering the plane, the electrodes generate a field. While physical demonstrations of the idea of a Paul trap use a rotating paraboloid surface, in our 2D cross-section, it is sufficient to identify a saddle point for a given static configuration of charges by the electrodes.[12] A simple example is shown in Fig. 4. In this case, two RF frequency electrodes are shown in a configuration with a periodic voltage applied. The central plate is a ground. The starred point shows a saddle point in the xy-plane. Upon applying an RF frequency to the trap, the saddle point at the star alternates, generating a pseudo-potential capable of trapping certain masses of ions.

In a predecessor to the IonQ case, the trap's radial frequency is $\omega_x = 3.07$ MHz, and the axial frequency is $\omega_y = 0.27$ MHz, which, in a smaller test case involving $m = 5$ ions, gives a spacing of approximately 5 μm.[9]

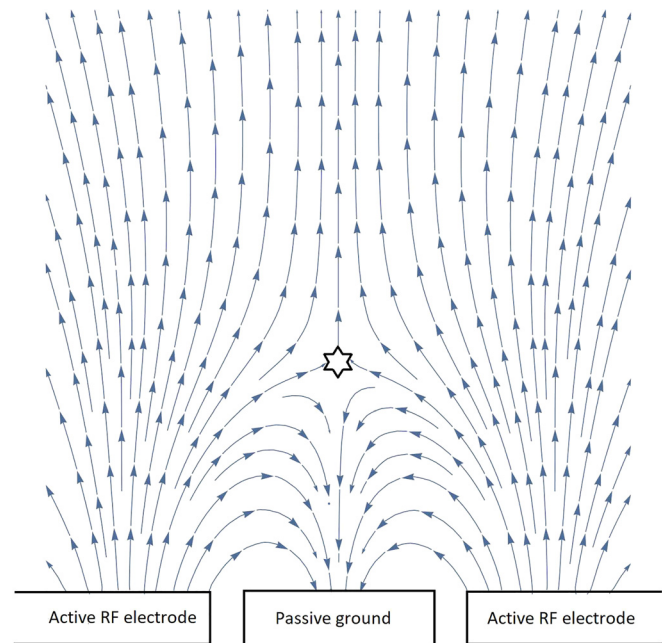| Active RF electrode | Passive ground | Active RF electrode |

Fig. 4. A cross section diagram of a potential electrode configuration. The saddle point is marked with a star. By using an RF voltage applied to the active electrodes, the saddle point can be alternated, creating a pseudo-potential to trap the ions enclosed.

1. Laser addressment and external apparatus

A recent IonQ design is shown in Fig. 5, where a view looking down from the positive y-axis is displayed. A global addressing beam illuminates the ions from the positive x-direction. From the negative x-direction, a single beam is split and modified both in frequency and amplitude by the multi-channel acousto-optical modulator (AOM) to implement SQs and TQs. The amplitude modulation switches individual beams on and off according to whichever pair of qubits should be entangled. Directly above the trap is a detection apparatus to sense individual photons, allowing for the measurement of the individual qubits at the end of a computation.

To make ion spacing more even for motional coupling, the ions at either end of the trap are left unused. However, as more ions are added to the ion trap, more symmetries start to be violated. The two primary considerations are unequal spacing and the appearance of a
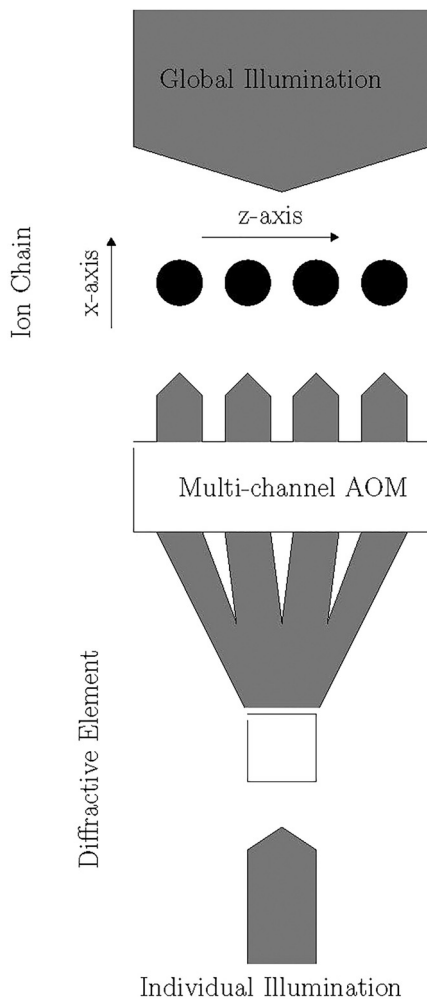

FIG. 5. A diagram of the IonQ quantum computer from the positive y vantage. The global and individual beams illuminate the ions to implement a variety of gates, discussed in Sec. VIII B. The ions are trapped in an ion trap perpendicular to the illumination.
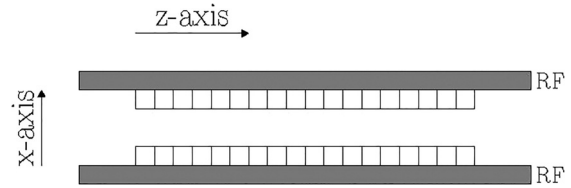

FIG. 6. A schematic from the positive y-direction of an IonQ ion trap design. Note that only the electrodes are shown. Here, the two RF electrodes aligned with the z axis are defined as in Sec. III A. The additional electrodes above and below $x = 0$ are used for ion positioning and placement. IonQ's Sandia-developed High Optical Access (HOA) trap has the electrodes inside the RF rails. Note that the ion junctions are not used, and not shown.

zigzag structure, as ions begin to form ion trap crystals, potentially causing modes to cross in sideband addressment, significantly decreasing the efficacy of gates. This causes anharmonic terms to appear, initiating a frequency shift in mode addressal.[13,14] IonQ makes use of anharmonic potential to deal with this, as discussed in Sec. VI A.

B. Paul trap ion locomotion

In Sec. III A, we assumed a simple ion trap design. However, finely tuned ion control is needed. IonQ could reposition ions to apply gates more uniformly in the limit as the number of ions in the trap increases. In the Sandia case, quasi-static electrodes are necessary to vary the length of the potential well and ensure that the bottom is sufficiently flat for optimal ion placement.[15]

Honeywell takes a different approach. Rather than positioning the electrodes evenly, they choose a denser configuration where advanced ion transport schemes are required, and a sparser configuration for ion transport. Between interactions, the ions are stored in memory regions. The electrodes then propel them through the central region in order to implement the gates (Fig. 6). Depending on the network's topology, arbitrary pairs of qubits can be shuttled to the interaction region in any desired arrangement, without the need to deal with multiple ions passing each other.

Referring to Fig. 7, specific zones are as follows:

(1) T designates auxiliary electrode blocks to maintain spacing between ions and transport them;
(2) A designates addressal electrode blocks used for advanced qubit operations such as transportation, gates, and storage. For transportation, a denser electrode configuration is used, discussed in Sec. VI B; and
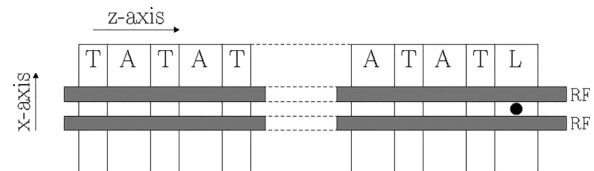(3) L designates the loading zone, where qubits are introduced through the single hole.

FIG. 7. A schematic from the positive y-direction of the Honeywell trap design. Here, electrode blocks are labeled according to their role in ion manipulation.

A total of 196 electrodes were used. The device was configured in a 2D arrangement with no line of sight between electrodes and ions.[7] Deterministic rotation of ion pairs with the electrodes eliminates the need for error-prone TQ logical swap gates.

Electrode shielding helps to eliminate unwanted interaction between ions and electrodes. The entire device is cooled to 12.6 K by the use of a cold finger attached to liquid helium.[7] The ions are suspended 90 μm above the surface, and all addressing beams are in the xz-plane of the trap surface. The ion trap in the Honeywell device operates with 190 V at 43.35 MHz for radial containment, the ion trap frequencies for a single Yb being $2\pi \times 0.97$, $2\pi \times 2.7$, and $2\pi \times 2.8$ MHz for the x-, y-, and z-axes, respectively. This additional constraint along the axial direction forms ion crystals of Ba^+ and $^{171}Yb^+$. The final four-ion crystal, which is used in the TQ gates, is 8 μm long.[7]

Laser addressing is at the level of single ion crystals. These are composed of either Yb–Ba–Ba–Yb or Ba–Yb–Yb–Ba for TQ traps, or otherwise just Ba–Yb, which is taken as a primitive unit throughout the computation.

IV. ION COOLING

The gates in ionic quantum computation are implemented by linking the electronic states with the motional states through a modified Hamiltonian that is facilitated by optical illumination. In order to keep the motional states from interfering with the qubit states, the atoms must be cooled to near zero-point energy in the Lamb-Dicke regime. The primary methods of interest are Doppler cooling and resolved sideband cooling with the option to use stimulated Raman transitions. Doppler cooling is applied at the initial stage to bring the atomic temperature quickly down to the Lamb-Dicke regime, after which resolved sideband methods are employed.

A. Theory

1. Doppler cooling

Doppler cooling in a single dimension for a trapped ion involves the illumination of the ion along the direction of its motion by a laser red-shifted to a chosen transition frequency. Atoms moving toward the light source will be more likely to absorb the light and receive a kick from the photon momentum. Emission is then in a random direction, causing an expected decrease in total momentum for the atom. The lowest temperature that can be achieved by this method is $\hbar\kappa/4k_B$, the Doppler temperature. Here, κ is the optical decay rate, and k_B is the Boltzmann constant.[16]

2. Lamb-Dicke regime

Henceforth, all calculations and explanations will assume that the ions addressed are in the Lamb-Dicke regime $\eta^2(2n+1) \ll 1$ with η as the Lamb-Dicke parameter given by $\eta^2 = \omega_R/\omega_z$, where ω_z is the axial frequency and $\omega_R = \hbar k_z^2/2m$ is the recoil frequency. Here, $k_z = \frac{2\pi}{\lambda}\cos\theta$ is the projection of the light's wavevector on the z-direction with λ the wavelength and θ the angle between the z-axis and the direction of the wavevector. We use the single degree of freedom approximation; note that the Lamb-Dicke regime assumption is required along each axis.[17]

In the Lamb-Dicke regime, the spontaneous decay of the ion occurs primarily at the frequency of the qubit's internal transition $|1\rangle - |0\rangle$. The insignificance of the coupling between motional and electronic states renders transitions of $|\Delta n| > 1$ improbable.

3. Resolved sideband cooling

The distinction between Raman sideband cooling and Doppler cooling is the relation between the frequency $\omega = (E_{|n\rangle} - E_{|n-1\rangle})/\hbar$ of the atom (with $E_{|n\rangle}$ being the energy of the atom in motional state $|n\rangle$, modeled as a simple harmonic oscillator) and the radiative linewidth γ. In the case of Doppler cooling, we have $\gamma \geq \omega$. For Raman sideband cooling, we require $\gamma \ll \omega$ to precisely target the secular motion of the ion. Then, if the atom has frequency $E_{|n\rangle}/\hbar = \omega_{tot}$, the laser can be tuned to the red sideband $\omega_{tot} - \omega$. The atom absorbs photons with energy $\hbar(\omega_{tot} - \omega)$ and emits photons with an average energy of $\hbar\omega_{tot} - (\hbar k)^2/2m$, where k is the wavevector of the emitted photon. Here, $(\hbar k)^2/2m$ is the recoil energy of the atom and is derived from $p_{light}^2/2m$ with $p_{light} = \hbar k$. In the case that $(\hbar k)^2/2m \ll \omega$, this corresponds to an expected decrease in energy of $\hbar\omega = E_\Delta$. To accelerate the cooling process, stimulated Raman cooling is typically used.[17]

4. Resolved sideband cooling with stimulated Raman transitions

Resolved sideband cooling with stimulated Raman transitions, or stimulated Raman cooling, operates on the same basic principle as resolved sideband cooling. However, in this case, a virtual state is exploited. An E_D detuning from a third state $|3\rangle$ is made, so that jumps to the $|3\rangle$ state are suppressed as a result of the energy gap. A second beam has approximately the same E_D detuning. Together, these beams produce an E_Δ detuning, which couples to the motional state and decreases the ion's motional energy.[18] This is shown in Fig. 8. Note that Raman transitions are used substantially to implement all gates discussed in Secs. VII and VIII.

The optical wavelength of the light allows for precise specification of the addressing, without involving unwanted ions. Additionally, the $|1\rangle - |0\rangle$ energy gap, in this case $\sim$12 GHz, allows a uniform treatment of resulting Stark shifts which may be accounted for experimentally. Furthermore, due to the slight detuning of the wavevectors, a single laser source can be modulated, allowing close control of the relative phase induced in the ion.

B. Ion chains

In an ion chain, different modes of vibration can be addressed individually, driving ions at frequencies for each mode of vibration in turn.[19] (An example of the relative energies of these different modes is included in Fig. 9.) Alternately, multiple vibrational modes may be addressed simultaneously to decrease cooling times; this is the method used in the IonQ quantum computer.[20] In order to cool each mode, the chain is cooled first with Doppler cooling, which requires no specific tuning. Following this, IonQ alternates between cooling atoms via stimulated Raman transitions and optical pumping from $|1\rangle \rightarrow |0\rangle$.

The IonQ Raman sideband cooling protocol uses the same 355 nm lasers discussed earlier. Here, however, modulation is used to induce a stimulated Raman transition with the $|0\rangle$ and $|1\rangle$ states of the $^{171}Yb^+$ being used for the bottom states in the diagram in Fig. 8. Then,

$$\text{———} \quad |3\rangle$$

$$E_D$$

$$- - - - - - - -$$

$$\text{——} \; |1\rangle$$
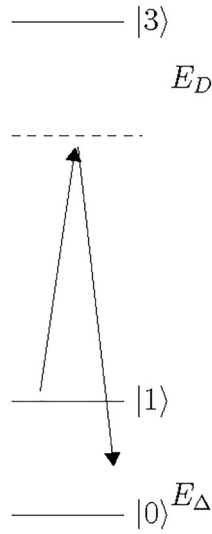
$$\text{———} \; |0\rangle \; E_\Delta$$

FIG. 8. Here, the basic process behind a stimulated Raman transition is illustrated. A given quantum state is illuminated by two beams simultaneously, so that the coherence time is relatively long compared to the interactions that we consider. The first arrow shows the first transition, which has a large E_D detuning from any other quantum state, decreasing the probability of transition to the point where it can be neglected. The second beam is then designed to give a small E_Δ detuning from $|0\rangle$. This creates the effect discussed in Sec. IV A 3.

$|3\rangle$ in this case is the $^2P_{1/2}$ state with sufficiently large detuning. The surrounding electrodes are used to rotate the normal mode coordinate about the z-axis such that only one set of transverse modes is addressable at a given time. In this case, the E_Δ is chosen to be the energy difference between two levels in the d-mode, namely, $|n_d, 0\rangle$ $-|n_d - 1, 1\rangle = E_\Delta$, by inducing the Hamiltonian $H^d = \Omega \eta_j^d$ $(\sigma_j^+ a_d + \sigma_j^- a_d^\dagger)$, where η_j^m is the Lamb-Dicke parameter for the d-mode and the j ion and Ω is the $|0\rangle \leftrightarrow |1\rangle$ frequency. Additionally, $\sigma_j^{+(-)}$ is the raising operator for jth ion, and a_d is the annihilation operator for ions in motional state m. Then, similarly to the induced Raman transition for sideband cooling, a length of time for illumination, τ, is experimentally determined in order to induce the $|n_d, 0\rangle \rightarrow$ $|n_d - 1, 1\rangle$ transition.

The primary innovation in the IonQ computer is that in a given ion chain, the η_j^d varies considerably. Through experimental

axial modes   transverse

0   1   2   3   4   5   6   7   8   9   10

FIG. 9. Phonon modes for the transverse and axial directions. Energies are given in ω_z units. The dashed line is the center of mass mode. In the current diagram, ten ions are used (as described in Ref. 38).

verification, a set of η_j^d that maximizes the cooling rate are chosen. Specifically,

$$\eta_j^i = \eta \, \cos\left(\frac{ij\pi}{m - 1}\right).$$

For each mode of vibration, there exists at least one antimode (labeled j_i) such that j_i is not an antimode of any but the center of mass mode. Then, for a given system $[1, ..., m]$ of qubits, we have a collection of M modes $[1, ..., m + 2]$, with two additional modes in this case corresponding to the two non-addressable ions at either end of the ion chain. The η_j^i can be computed, giving a matrix of values. Each of the m ions is coupled to an individual mode i based on the dual constraints of optimizing the η_j^i to maximize cooling, while guaranteeing that each mode is cooled.

Consider a toy example with four ions. Ion 2 might strongly drive mode 2 and moderately drive mode 1. Ion 3 might strongly drive mode 3 and moderately drive 4. In this case, the first cooling application would use η_2^2 and η_3^3, while the next two applications might use η_2^1 and η_2^1. Each ion uses a Raman transition to the mode with which it is most strongly linked.

Previous single mode cooling schemes required $O(m)$ time, scaling linearly with the number of ions for each mode that needed to be cooled. The new method is shown empirically to require $O(\sqrt{m})$ time, namely,[20]

$$\max_i\left\{\left|\cos\left(\frac{ij_i\pi}{m - 1}\right)\right|^{-1}\right\}\left(\frac{\pi}{2\Omega\eta}\sum_{n=1}^{M}\frac{1}{\sqrt{n}}\right).$$

In this case, cooling is applied before a computation, as the optical pumping inevitably destroys qubit states.

C. Barium

The Honeywell device uses resolved sideband cooling. Rather than cooling the ytterbium ion directly, the barium ion is cooled to avoid interference with the qubit states. In order for sympathetic cooling to be efficient, the masses of the ions must be similar, prohibiting the use of lighter ions such as Be^+.[21,22] This allows cooling to take place during the run of the quantum computer via sympathetic cooling. The Honeywell machine cools ions to near zero point energy before each gate application during a computation.

Honeywell report that 493.5 nm laser light was applied to the $^{138}Ba^+$ ion. This would seem to indicate the use of a simple resolved sideband cooling with ϵ detuning. However, this method is likely to run foul of being trapped by the metastable $^2D_{3/2}$. The cooling time is relatively long.

Stimulated Raman transitions are possibly implemented in the Honeywell computer, being known to work well in other similar arrangements. In the case of even Ba^+ ions, there is no hyperfine structure. Zeeman splitting does occur and is imposed on the ions, corroborating the need for a magnetic field to quantize the qubit.[23] For initial cooling of the $^{138}Ba^+$ ion, typical Doppler cooling methods are used, as indicated in the Appendix. Here, the $6S_{1/2}$ Zeeman levels are separated by 10.97 MHz with a field of 3.919 G. Light at 493.5 nm resonates with the $^2S_{1/2} \leftrightarrow 6\,^2P_{1/2}$, while $^2P_{1/2} \leftrightarrow 5\,^2D_{3/2}$ forms a 649.9 nm transition.
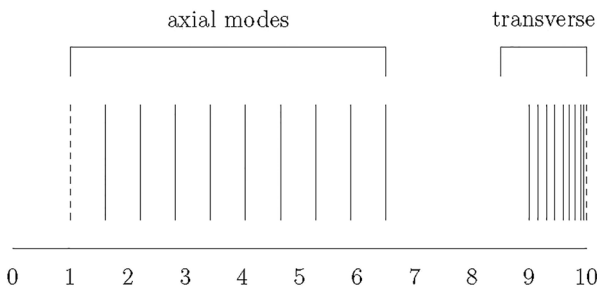
The $^2P_{1/2} \leftrightarrow {}^2D_{3/2}$ transition is possibly illuminated to depopulate the $^2D_{3/2}$ level. Note that the $^2P_{1/2} \leftrightarrow {}^2D_{3/2}$ illumination scheme is an optional repumping, which may be used in either the resolved sideband or stimulated Raman cooling schemes.

For Doppler cooling, as in Fig. 10, the beam is taken at 493.5 nm with no detuning. This is applied for 20 ms. No data are available for what the average motional state $\bar{n}$ is after Doppler cooling.

The $6\,^2S_{1/2} \leftrightarrow 6\,^2P_{1/2}$ modulated laser is passed through two AOMs, which convert the frequency by $+160$ MHz and -80 MHz. The resulting Raman probe beam has a Rabi frequency of $\Omega_{\text{probe}} = 2\pi \times 1.07$ MHz with an effective Rabi frequency of $2\pi \times 89$ kHz. The Raman σ^+ polarized light has a Rabi frequency of $2\pi \times 14.9$ MHz. This provides a frequency difference slightly red-detuned to the Zeeman gap and a gap from the $6\,^2S_{1/2} \leftrightarrow 6\,^2P_{1/2}$ electronic transition of $\Delta = 2\pi \times -79$ MHz. The values were determined experimentally.[23] The procedure results in the cooling of the ^{138}Ba$^+$ ion to $\bar{n} = 0.17$.

V. QUBIT INITIALIZATION AND DETECTION

The ^{171}Yb$^+$ ions have a reasonably standard method of initialization and readout, using the hyperfine to optical coupling with S–P transitions. To maintain fidelity, illumination of the $^3D[3/2]_{1/2} \leftrightarrow {}^2D_{3/2}$ with a large-bandwidth laser reduces the possibility of metastable trapping of the electron outside the desired transitions.

The ^{171}Yb$^+$ qubit initialization is achieved by optical pumping, as illustrated in Fig. 11. Dotted lines denote natural lines of decay, while solid lines denote the illuminated transitions.

In the case of optical pumping for ^{171}Yb$^+$, two resonances are used. The first is a laser tuned to the $^2S_{1/2}|F=1\rangle \leftrightarrow {}^2P_{1/2}|F=0\rangle$ gap at 369.53 nm. This beam, before illuminating the ion, is passed through a 2.1 GHz electro-optic modulator, which is switched on during initialization to generate a positive first-order sideband resonance with the $^2S_{1/2}|F=1\rangle \leftrightarrow {}^2P_{1/2}|F=1\rangle$ transition. Once an electron is pumped from $|1\rangle$ to $^2P_{1/2}$, it has a 1/3 chance of falling directly to $|0\rangle$. However, it is also possible for the electron to fall to the metastable $^2D_{3/2}$. To combat this, an additional beam is used to illuminate the ^{171}Yb$^+$ at the $^2D_{3/2}|F=2\rangle \leftrightarrow {}^3D[3/2]_{1/2}|F=1\rangle$ transition. This is accomplished by an electro-optic modulator at 3.07 GHz to produce
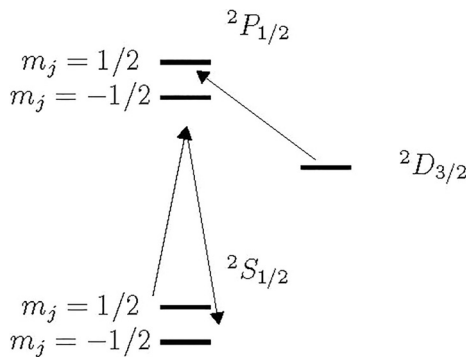
935.2 nm light. This drives the states to $^3D[3/2]_{1/2}$, which then rapidly decay to $^2S_{1/2}$. States which decay to $|1\rangle$ are rapidly repumped through the cycle. A near perfect state initialization to $|0\rangle$ is achieved in less than 0.5 μs.

A. Qubit readouts

The qubit is readout through similar fluorescent techniques, shown in Fig. 12. Here, the significance of the dashed and solid lines remains the same as in Fig. 11.

The procedure for fluorescence is similar to that used for state initialization. Again, 369.53 nm light is tuned in resonance with the $^2S_{1/2}|F=1\rangle \leftrightarrow {}^2P_{1/2}|F=0\rangle$ transition. This pumps the electrons in $|1\rangle$ almost exclusively, as the transition $|0\rangle \leftrightarrow {}^2P_{1/2}|F=1\rangle$ is detuned by 14.7 GHz. Any electrons in $^2D_{3/2}$ are then pumped and decay to the ground state, emitting photons.

In the cyclic coupling of the $|1\rangle$-state and the $^2P_{1/2}|F=0\rangle$ state, when counting the number of photons emitted as a result of detection, there is a Poisson distribution, as a result of off-resonant coupling to the $^2P_{1/2}|F=1\rangle$-manifold. The splitting of the $^2P_{1/2}|F=0\rangle \leftrightarrow {}^2P_{1/2}|F=1\rangle$ gap is approximately 2.1 GHz. Take λ_0 to be the mean number of counted photons, τ_D to be the average detection time, η to be the detection efficiency, i.e., the number of photons detected per number of photons emitted, and τ_L to be the average time of leakage from the $|1\rangle \leftrightarrow {}^2P_{1/2}|F=0\rangle$ states to the $|0\rangle \leftrightarrow {}^2P_{1/2}|F=1\rangle$ states. Using the Poisson distribution and setting $\alpha = \frac{\tau_D \eta}{\tau_L \lambda_0}$, we have a probability

$$p(n) = \frac{e^{-(1+\alpha/\eta)\lambda_0}\lambda_0^n}{n!} + \frac{\alpha/\eta}{(1+\alpha/\eta)^{n+1}}\frac{1}{n!}\int_0^{(1+\alpha/\eta)\lambda_0} e^{-y}y^n\,dy$$
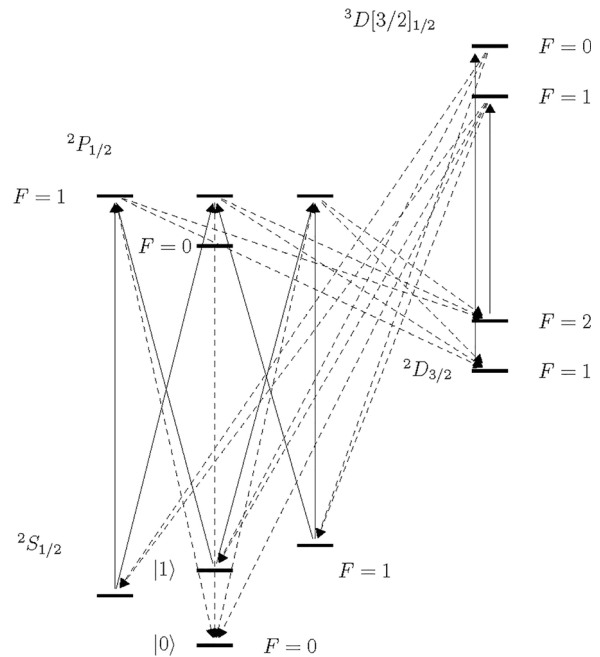
FIG. 11. ^{171}Yb$^+$ qubit initialization by tuning the p and s orbitals. All other levels are for depumping. Here, solid lines represent induced transitions, while dotted lines represent spontaneous transitions. Adapted with permission from Olmschenk *et al.*, Phys. Rev. A **76**, 052314 (2007). Copyright 2007 American Physical Society.

FIG. 10. ^{138}Ba$^+$ stimulated Raman cooling. Here, Δ discussed before is chosen to be below the $^2P_{1/2}$ state with an ϵ detuning between the m_j Zeeman levels in the s state. As with the Doppler cooling, an additional beam is needed to prevent trapping and to allow the cooling cycle to continue. Only relevant layers are shown; states $^2P_{3/2}$ and $^2D_{3/2}$ were excluded.

FIG. 12. ^{171}Yb$^+$ qubit readout. Note the similarities with Fig. 11. Solid lines represent induced transitions, while dotted lines represent spontaneous transitions. Adapted with permission from Olmschenk et al., Phys. Rev. A **76**, 052314 (2007). Copyright 2007 American Physical Society.

of detecting n photons. Then, the detection probability is $1 - p(0)$ using a one-photon threshold for deciding if the qubit is in the $|1\rangle$-state, which for ^{171}Yb$^+$ has been calculated to be 0.9933 for $\eta = 0.001$.[24]
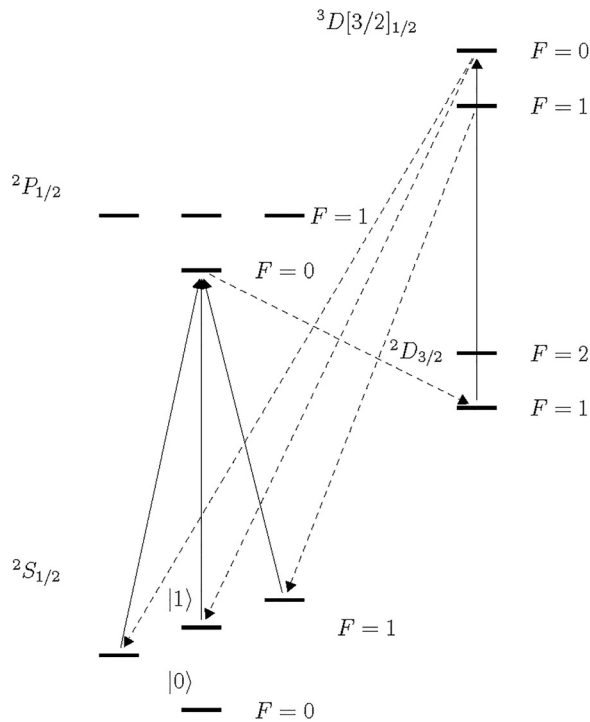
This accounts for the majority of the error. However, additional error may result from coherent population trapping, where a photon is coherently manipulated by the detection scheme and trapped in the $|1\rangle$-manifold. Modulation of the polarization of the light during addressing can be used to reduce the probability of coherent manipulation of the qubit to a 1/3 chance of being trapped each cycle without photon emission. However, this merely increases the expected time of optical pumping until a photon is detected.[25] The main limitation is aperture detection efficiency. With an aperture efficiency of 0.001, the maximum theoretical state detection fidelity is 0.9855, while for an aperture efficiency of 0.1, state detection fidelity can reach 0.999 85. In practice, Noek et al. demonstrated 0.998 56 fidelity with an average detection time of 28.1 μs.[26]

VI. ION TRANSPORT

A microfabricated linear ion trap with electrodes offers several convenient features. Many quantum computers have significant issues with cross-correlation errors between qubit gates when implementing SQ and TQ gates simultaneously, which are not easily resolved. In the Honeywell computer, memory qubits can be moved a significant distance away from operating TQ gates, rendering such cross-talk errors

statistically insignificant. Furthermore, qubits may be interchanged physically, eliminating the need for a logical implementation with swap gates.

All of the control methods discussed here maintain the ions at a distance from the electrodes that is significantly larger than the distance between the ions themselves. This allows the surrounding apparatus to remain at a higher temperature than might otherwise be acceptable (12.6 K in the Honeywell configuration).

A. Qubit string modulation

As discussed at the end of Sec. III A 1, IonQ uses an anharmonic potential to achieve uniform ion spacing in the crystal in use. We present a treatment that utilizes a feedback method to create a long equidistant ion string with control over potential depth and ion distance.[27]

The ith ion in an ion string experiences a Coulomb interaction

$$E_i = \frac{q}{4\pi\epsilon_0} \sum_{j\neq i} \frac{z_i - z_j}{|z_i - z_j|^3},$$

with the $m-1$ remaining ions j. To counter-balance this interaction, an analytic solution to the surface potential for each rectangular electrode may be written as

$$\Phi_j(V_j, x, y, z) = \frac{V_j}{2\pi} \left[\arctan\left(\frac{(x_{j2} - x)(z_{j2} - z)}{y\sqrt{y^2 + (x_{j2} - x)^2 + (z_{j2} - z)^2}} \right) \right.$$
$$- \arctan\left(\frac{(x_{j1} - x)(z_{j2} - z)}{y\sqrt{y^2 + (x_{j1} - x)^2 + (z_{j2} - z)^2}} \right)$$
$$- \arctan\left(\frac{(x_{j2} - x)(z_{j1} - z)}{y\sqrt{y^2 + (x_{j2} - x)^2 + (z_{j1} - z)^2}} \right)$$
$$\left. + \arctan\left(\frac{(x_{j1} - x)(z_{j1} - z)}{y\sqrt{y^2 + (x_{j1} - x)^2 + (z_{j1} - z)^2}} \right) \right],$$

using (x_{j1}, z_{j1}) and (x_{j2}, z_{j2}) as the coordinates of the opposing electrodes in the $y = 0$ plane.[28] We can combine these potentials as $\Phi(x, y, z) = [\Phi_j(1, x, y, z)]_j V$, where V is the vector of voltages. Then, we can balance the equation for the ions by requiring the force of the potential to counter the force of the individual ions on each other. Writing this out gives the following equation:

$$\left[-\frac{\partial \Phi_j(1, 0, y_c, z)}{\partial z}\bigg|_{z=z_i} \right] V = -E_I,$$

where E_I is the vector of Coulomb interactions experienced by each ion and y_c refers to the height of the electrodes about the surface trap. This equation is subject to suitable constraints on the voltages. Setting $F = \left[-\frac{\partial \Phi_j(1,0,y_c,z)}{\partial z}\big|_{z=z_i} \right]_{ij}$ and choosing a two-norm to equalize the ion distances, we obtain the optimization problem,

$$\text{argmin}_V (V^T F^T F V + 2F^T E V),$$

which may be solved quadratically.

In the solution so far, the generated electric field E_I for the ions is calculated independently of the ion positions and left constant during the calculation. By applying a field control modification of order $F\Delta V \sim \Delta E_I$, where ΔE_I denotes the desired difference in electric field and ΔV denotes the amount of modification, it is possible to generate a flat potential. At each stage, the relative ion positions are measured using florescence to guide subsequent iterations of the feedback.[27]

B. Qubit transport

While adiabatic transport of qubits is possible, diabatic transport is much faster. Adiabatic transport acquires phase dependence due to field imhomogeneity, which can be mapped experimentally, and then compensated in subsequent computations. However, qubits acquire a path- and time-dependent phase based on the speed of transport. The DC Stark shift, which can affect the internal states of the qubits, may be ignored here due to the insulation of the electronic fields in $^{171}Yb^+$.

Theoretically, the RF field containing the ions and the field due to the electrodes may be approximated by a particle in a quadratic potential well for ions with low motional energy. Thus, the Hamiltonian,

$$H = \frac{p}{2m} + \frac{1}{2}m\omega^2(x - s(t))^2,$$

may be used to describe the ion's motion, with ω being the harmonic frequency of the potential well formed by the electrostatic fields. Here, $s(t)$ represents the center of the well as a function of time in 1D space, and the other variables are standard.[29] Replacing the wavefunction $|\psi\rangle$ by a wavefunction $|\chi\rangle$ displaced by $s(t)$ with an appropriate displacement operator, the Schrödinger equation becomes

$$i\hbar|\chi\rangle = (H_0 + \dot{s}(t)p)|\chi\rangle,$$

where H_0 gives the untranslated harmonic oscillator.

Under the assumption that the initial state of the oscillator is the ground state, so that $|\psi\rangle = |0\rangle$, we can solve the equation for the amplitude $\alpha(t)$ as

$$\alpha(t) = \sqrt{\frac{m\omega}{2\hbar}}\left(s(t) - e^{-i\omega t}\int_0^t \dot{s}(u)e^{i\omega u}du\right),$$

with $|\psi\rangle = |\alpha(t)\rangle$.

The goal then is to leave the particle in the ground state or near it. This is equivalent to minimizing

$$\alpha(t) - \sqrt{\frac{m\omega}{2\hbar}}s(t) = \sqrt{\frac{m\omega}{2\hbar}}e^{-i\omega t}\int_0^t \dot{s}(u)e^{i\omega u}du.$$

By setting $s(t) = v$ for $t \in [0, t_T]$ and 0 otherwise, the equation can be solved as

$$\frac{iv}{\omega}(1 - e^{-i\omega t_T})\sqrt{\frac{m\omega}{2\hbar}},$$

which becomes 0 when $\omega t_T/2\pi$ is an integer. Since the solution is oscillating, even for non-ideal motion, a simple numerical calculation shows how the ion may easily be brought back to the ground state for reasonably high ratios of ω to the transport distance of the ion.[30]

In addition, the qubit acquires a local phase during transport. To account for the phase shift, neglect the global phase

$$\alpha|0\rangle + \beta|e\rangle \longrightarrow \alpha|0\rangle + \beta e^{i\phi}|e\rangle.$$

Perturbation theory, utilizing a time-independent assumption, gives

$$\phi = \frac{m^2}{\hbar}\left(\sum_{m\neq|0\rangle}\frac{|\langle m|X|0\rangle|}{\hbar(\omega_{|0\rangle} - \omega_m)} - \sum_{m\neq|e\rangle}\frac{|\langle m|X|e\rangle|}{\hbar(\omega_{|e\rangle} - \omega_m)}\right)\int_0^T \ddot{\alpha}(t)^2 dt.$$

This is calculated and numerically held to 0, except for gate action, by the intermediary processor which controls the electrodes.

C. Ion separation

Separation and combination of four-ions into a pair of two-ions and vice versa are accomplished with an octopolar electric field. Assume that the relevant qubits are contained by an RF-field, which is symmetric in the y, z-coordinates. Then, the goal is to use the electrodes in the QCCD architecture that line the trap to generate a potential field, as illustrated in Fig. 13.

Here, the ions are at $\pm\delta$ by assumption. First, we write the potential out in terms of its Taylor expansion

$$V(x, 0, 0) = V_0 - E_0 x + \alpha x^2 + E_1 x^3 + \beta x^4.$$

Then, as a simplifying assumption, we work with the case in which the electrodes are symmetric. We motivate this by noting that an asymmetric component of the separating field would push both ions to one side of the well. Our assumption allows us to remove the cubic term. The assumption that there be two wells forces $\alpha < 0$ and $\beta > 0$. For $E_0 \sim 0$, we realize that $\partial V/\partial z = 0$ gives

$$s = \sqrt{\frac{|\alpha|}{2|\beta|}}.$$

If we assume that $V(x, 0, 0)$ is constant in time, then

$$-\alpha = \frac{m\omega_x}{4q},$$

with ω_x as the frequency of the ion.

To preserve qubit coherence, it is desirable to minimize higher-order terms in the expansion of the electric field. In order to
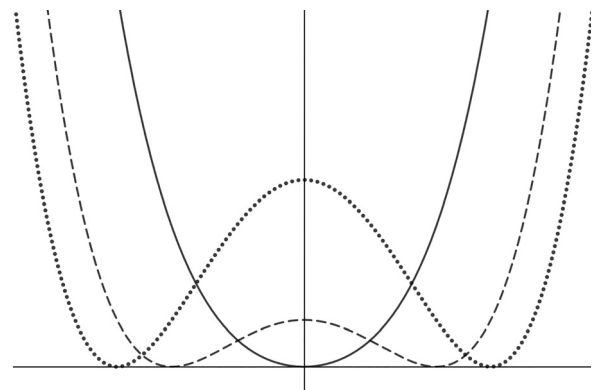

FIG. 13. Qubit separation potential, assumed to be symmetric. The local maximum is increased until the ions are separated. The symmetry assumption guarantees that a quartic order term alone achieves ion separation. Here, the potential for ion separation is shown. The time sequence for the lines representing potential is in the order solid, dashed, and dotted.

accomplish this, it is convenient to space the electrodes as far from the ions as is possible.[32] Now, if a is the minimum distance from the electrodes to the ions, we have $\alpha/\beta \ll a^2$.[31] We take $\alpha = 0$, implying that it is possible to have an electric configuration in which the second derivative is zero and the quartic is non-zero. Laplace's equation gives $\partial^2 V/\partial y^2 = -\partial^2 V/\partial x^2$, implying that the field strongly repels in some direction in the xy-plane. If an oscillating field is chosen, one type of Paul trap design, then the effective values of α and β are reduced. Thus, it is necessary to produce an octopole. The desired potential field is

$$V(x, y, z, t) \sim \alpha(z^2 - (x^2 + y^2)/2) + \beta z^4 + Q_{ac}\cos(\Omega t)(x^2 - y^2).$$

In order to achieve the required electric field configuration, at least six electrodes are necessary. For an order 4, symmetric 2D array, the configuration in Fig. 14 demonstrates an appropriate method for generating the initial octopolar moment.

D. Ion swapping

Ion swapping occurs when a string of ions rotates about an axis orthogonal to the RF-null axis. This specific maneuver is necessary for the transport of ions between locations as well as to maintain symmetric TQ gates composed of the two different ion types,

$$Yb-Ba-Ba-Yb \quad \text{and} \quad Ba-Yb-Yb-Ba.$$

The Honeywell literature includes a complete description for a one-point and a three-point turn for the ions involved. We will visit the one-point turn in depth and merely give a brief description of the technique behind a three-point ion turn.[33]

The basic configuration for the ion swapping procedure is illustrated in Fig. 15. Note the labeling in the figure. There are three configurations applied to the A–D electrodes,

(1) electrode z-balance: A: $+$, B: $-$, C: $+$, D: $-$,
(2) electrode x-balance: A: $-$, B: $-$, C: $+$, D: $+$, and
(3) electrode diagonal: A: $-$, B: $+$, C: $+$, D: $-$.

In order to flip the qubit, first, the side voltages are relaxed, while the endcap voltages increase, increasing the range of movement in the zx-plane, rather than imposing linear motion.
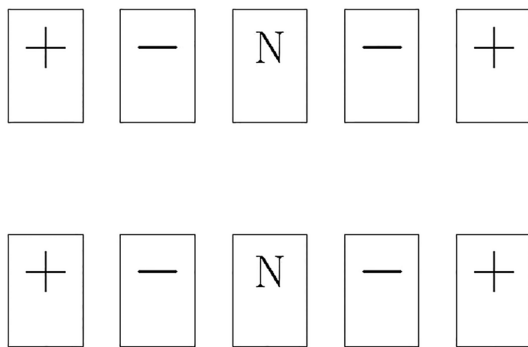

FIG. 14. An example of a linear design with the necessary quartic term. Here, the relative charges are demonstrated. These charges would occur halfway through the separation process. The two central neutral charges might also be slightly positive. The minimal set of relevant electrodes is shown.
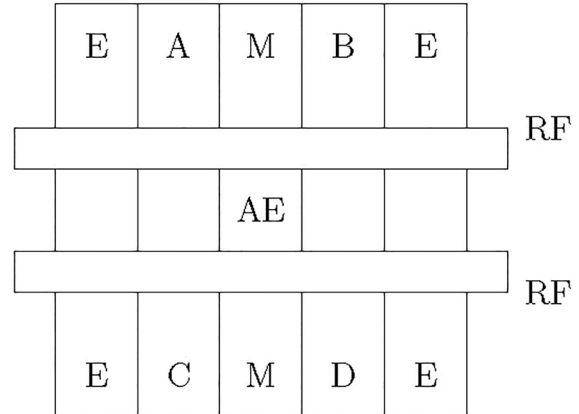

FIG. 15. Electrode configuration for ion-swapping on the z-axis. The end cap electrodes are denoted as E, midpoint electrodes are denoted as M, and the rotational electrodes are labeled as A–D. The entire setup requires the crystallized ion string to be centered above the AE electrode in order to complete a rotation. The other electrodes that appear in the Honeywell architecture (Fig. 7) serve for manipulation in the y- and x-axes (as described in Ref. 33).

While this happens, the primary means of controlling the direction of rotation is first applying a positive electrode diagonal, then a negative electrode diagonal as the endcap and planar electrodes are returned to their original states. This creates diagonal wells along the $x = -z$ and then along the $x = z$ directions, meaning that the ion string aligns itself $x = 0$, $x = -z$, $z = 0$, $x = z$, $x = 0$, which completes a rotation of π. Using components of the z-balance and x-balance, a hinge in the ion string may effectively be chosen, positioning the ion chain in the z- and x-directions. The relative voltage signatures and ion motions are depicted in Fig. 16.

Experiments were performed on pairs of ions. The Ba ions were pumped to an appropriate ground state and then excited using the technique mentioned above. The fidelity was 0.97 after 433 trials. The fidelity of the swap had no time dependence over the interval [1.5 ms, 20 ms]. Below this time, the fidelity dropped rapidly due to imperfections in how the low pass filters modulated the waveform applied to the electrodes. Heating equivalent to at most one quantum of the motional mode was predicted.

A three-point ion turn, analogous to a three-point turn of a car, is also proposed in Ref. 33. By pushing the ion out of the center with increased electrode z-balance and x-balance, it is possible to avoid the center of the apparatus where various changes may occur that are unpredictable and hard to compute.

Honeywell clarifies that their sorting time length is of order $O(m)$. Any algorithm which requires that only one swap be implemented at a time is bounded below by an $O(m \log m)$ time. Parallel models can implement $O(m)$ time sorts. This indicates the benefits of a dense electrode configuration, scaling the number of simultaneous swaps with the number of ions. This is efficient if $\sim m/2$ TQs are implemented after each transport cycle with classical sorting costs being ignored. Totally connected systems with simultaneous gate applications are faster, although, to our knowledge, no experimental demonstration of a scalable high-fidelity simultaneous application scheme exists.
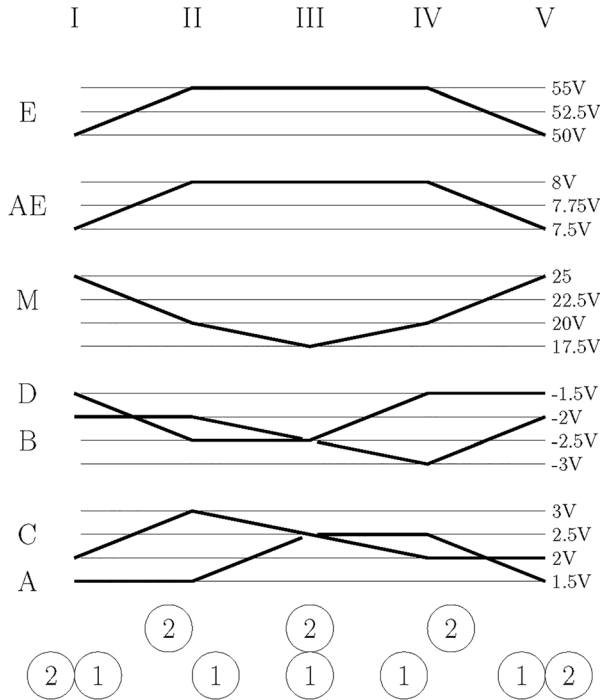
FIG. 16. A sample of electrode voltages for Fig. 15. Reading from left to right gives the five-step time sequence of charges with the ion positions being shown along the bottom throughout the operation for the qubit swap. The general shapes of the AC and BD paths are piecewise convex and concave curves, respectively. If an iso-charge surface of the electric field was chosen, it would form an elliptically distended paraboloid with the z axis as the initial major axis, rotating with time (as described in Ref. 33).

VII. SINGLE QUBIT GATES

The Honeywell machine uses separate implementations for the X, Y, and Z qubit rotations. The X and Y qubit rotations are implemented with commonly used techniques.[8] A stimulated Raman transition is induced to implement the gates with copropagating waves. This is identical to the procedure described in Sec. IV A 4, although in this case $E_\Delta = 0$, as no change in the motional state is desired. Additionally, induction of a phase in the transport of an ion occurs as described in Sec. VI. IonQ does not explicitly state their methodology here, but a similar method would work for SQ's without the complexities due to ion transport and off-resonant cooling.

The Z rotation is achieved with a numerical phase-tracking protocol implemented on a classical computer. It uses the phase accumulated during transport, differences in the magnetic field, and the AC Stark phase to determine the transport speed.[7] Qubit rotations are restricted to $\pi/2$ increments with a resolution of $\pi/500$.

VIII. TWO QUBIT GATES

While TQ gates can be realized in various ways, modern implementations rely primarily on variations of the Mølmer–Sørenson gate. The basic principle is similar in some ways to the stimulated transitions used in Raman cooling. Here, however, a dichroic light source is used to link the vibrational modes of two atoms. The first-order coupling is significantly stronger than higher coupling modes caused by

the absorption of multiple photons. As a result, a straightforward Hamiltonian is formed, which is used for a universal TQ gate. Bearing in mind the similarities between different gate types, we first examine the general notion of a Mølmer-Sørenson gate, before considering specific implementations.

A. Mølmer–Sørenson gate

Within the general trapped ion interaction scheme, Sørenson and Mølmer proposed solutions to the problem of implementing multi-qubit quantum gates unaffected by changes in the vibrational modes, as long as the internal states of the ions did not stray from the Lamb-Dicke regime.[34] The vibrational modes were accessed as intermediate states, but transition paths involving different modes interfered destructively to eliminate the dependence on them, applying Milburn's method of combining Hamiltonians to the ion-based picture.[34,35] Suppose that there are two given Hamiltonians H_1, H_2 controlled by real parameters κ_1 and κ_2, respectively. Furthermore, assume that these Hamiltonians are rapidly alternated in their application. Then, combining the corresponding unitary matrices gives

$$U_{tot} = e^{i\kappa_2 H_2 dt} e^{i\kappa_1 H_1 dt} e^{-i\kappa_2 H_2 dt} e^{-i\kappa_1 H_1 dt} = e^{\kappa_1 \kappa_2 [H_1, H_2] dt^2} + O(dt^3),$$

over a cycle. This realizes the Hamiltonian $i\kappa_1 \kappa_2 [H_1, H_2]$. Milburn treated a sample derivation with Hamiltonians XJ_z and PJ_z in terms of spin operators defined on $|g\rangle$ and $|e\rangle$ giving rise to the Hamiltonian $i[XJ_z, PJ_z] = J_z^2$, which is independent of both the position and momentum operators. This implies that the evolution of the system is independent of the spatial vibrational modes.

For general multi-qubit gates, Sørenson and Mølmer made use of individual lasers to address each qubit, as shown in Fig. 5. However, for TQ gates, they proposed a special scheme using detuned laser pulses directed along the axis of the trap, though Raman transitions are not necessary for the implementation. To improve the accuracy of the method, given the center of mass (CM) mode frequency ν, each laser is detuned from ν by a suitably large amount ϵ to avoid interference with other states. The "blue" laser addressing the first ion is detuned close to the upper sideband, thus close to resonance with a joint internal ion and vibrational excitation (Fig. 17). Write $|ab\,m\rangle$ for respective qubit states $|a\rangle$ and $|b\rangle$ at CM vibrational mode $|m\rangle$. The "red" laser addressing the second ion is detuned close to the lower sideband.

In the transitions,

$$|ggn\rangle \leftrightarrow \{|egn+1\rangle, |gen-1\rangle\} \leftrightarrow |een\rangle, \tag{1}$$

the intermediate states are not populated. Consider the case in which both ions are illuminated. Then, by analyzing the Hamiltonian using a second order expansion and perturbation theory, the Rabi frequency $\tilde{\Omega}$ for the transitions (1) is given by

$$\left(\frac{\tilde{\Omega}}{2}\right)^2 = \frac{1}{\hbar^2} \left| \sum_m \frac{\langle een|\sum_n H_{n,0}|m\rangle \langle m|\sum_n H_{n,0}|ggn\rangle}{E_{|ggn\rangle} + \hbar\omega_i - E_m} \right|^2$$

with $\omega_i = \nu \pm \epsilon$ and intermediate states m. Taking $|eg\,n+1\rangle, |ge\,n-1\rangle$ as the only intermediate states, the sum reduces to

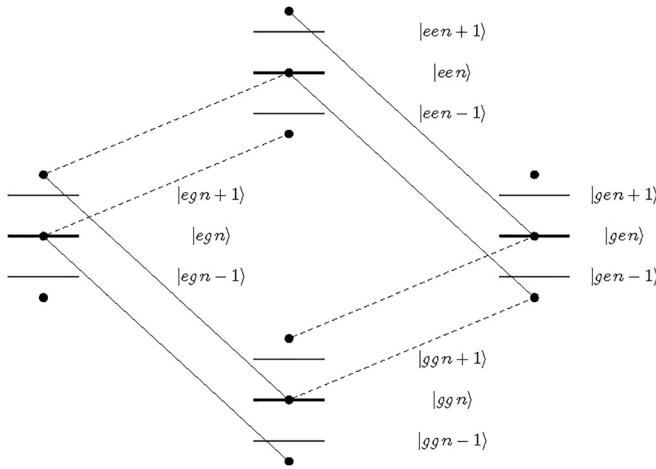$$\tilde{\Omega} = \frac{(\Omega\eta^*)^2}{2(\nu - \epsilon)}.$$

FIG. 17. A first order approximation for transitions between different energy states of the TQs in the Mølmer–Sørenson gate. The solid lines represent the blue-detuned light, while the dotted lines represent the red-detuned light. Detuning increases the probability that both beams act on the energy levels of the quantum system, as noted earlier in the discussion of the role of the stimulated Raman transitions.

The ν-detunings function in stimulated Raman transitions. The coupling to states which are exactly matched increases exponentially, while the coupling to unmatched states decreases. A full error analysis is available in Ref. 36. The Rabi frequency is independent of the excitations of vibrational modes of the ions, allowing the addressing of internal states alone. This determines the transition between the states $|gg\,n\rangle$ and $|ee\,n\rangle$ as depicted in Fig. 17.

B. Motion-mediated Ising gates

In order to minimize the effect of modal cross-talk on TQ operations in ion chains, the energy transitions between motional states should be small. Gates may be linked to two types of motional modes: axial and transverse. The axial mode is measured by the frequency of the center of mass of the ions along the length of the ion trap, while the transverse mode is measured by the frequency of the ion motion perpendicular to the ion trap. The modes are observed to obey a power law in the number m of ions in the ion string.

An IonQ experiment gave $\tau_g \gg 1/\omega_z > m^{0.86}/\omega_x$ for the axial mode, where ω_x is the transverse mode frequency and ω_z is the axial mode frequency. Similarly, $\tau_g \gg \omega_x/\omega_z^2 > m^{1.72}/\omega_x$ for the transverse mode. As a result, TQ gates are chosen to be implemented in the transverse rather than the axial direction.[37,38]

One of the initial benefits of coupling ion motional states directly to the hyperfine states is the easy arbitrary linkage that is available by selectively illuminating any chosen pair of qubits. IonQ has the maximum possible connectivity, which allows implementation of TQ gates on arbitrary qubit pairs. However, two crucial speed limitations make their impact. While ion chain TQ schemes have demonstrated simultaneous gate application, fidelity tends to be reduced. For instance, on an IonQ device, five sequential gates had a fidelity of $\sim$0.92, while reimplemented concurrently, the gates had fidelity of $\sim$0.88.[37] Furthermore, fractional power dependency of the gate times on the

number of ions quickly decreases the speed and efficiency of larger quantum systems.[39]

IonQ achieves its full connectivity with a multi-channel AOM counterpropagating along the x-axis over the trap surface (Fig. 5). The laser is split into two beams. One of the beams illuminates the entire ion chain. The other is channeled into individual beams with a 3.5 μm waist for each ion. Ions are addressed by two counterpropagating lasers: one oriented in the $+x$ direction, the other in the $-x$ direction. The light sources have a frequency detuning μ which is used to generate Raman transitions.

To eliminate the total force applied, AOMs produce a bichromatic illumination at $\omega_0 \pm \mu$, where $\mu \sim \omega_x, \omega_z$ depending on the motional wave being coupled. Since all operations are performed in the Lamb-Dicke regime, we may use the rotating wave approximation $U(\tau) = \exp[\sum_i \phi_i(\tau)\sigma_x^i + i\sum_{i,j}\chi_{i,j}(\tau)\sigma_x^i\sigma_x^j]$. Here, σ_x^i is the Pauli-X operator on the ith qubit defined relative to the phase of illuminating beat notes. Then, $\phi_i(\tau)$ is the corresponding raising operator on the mode, and $\chi_{i,j}(\tau)$ represents the entangling interaction between qubits. A full description of these variables is given in Ref. 38.

Together with arbitrary SQs, the XX-gate $U_{XX} = \exp\left(-i\frac{\pi}{4}X \otimes X\right)$ generates a universal gate set. It is implemented as $U(\tau_g) = \exp[i\pi\sigma_x^a\sigma_x^b/4]$ between an arbitrary pair a and b of qubits. Thus, it is necessary to have $\chi_{a,b}(\tau_g) = \pi/4$, while all other components of the Hamiltonian should vanish at time τ_g. In order to match this system of constraints, the laser's pulse package can be split into components that are evenly spaced in time, and separately modulated to satisfy the resulting system of linear equations.

Normal laser output is achieved by using semi-mirror ends on a cavity, such that only certain frequencies of light constructively interfere upon rebound. Under regular laser operation, the relative phases of these frequencies are random and, depending on the number of resonant frequencies generated, can cause either a pulsing behavior or generate an almost constant stream of light. There are several methods to choose the different resonant frequencies of laser light. For the XX-gate, a series of stimulated Raman transitions are created through the simultaneous addressing by two phase-locked lasers, as depicted in Fig. 18. The frequency and phase of the lasers are modulated by an AOM to deliver a pack amplitude so that beats occur only when a gate has to be implemented. The mode-locked lasers emit a rapid sequence of frequency comb pulses, where the frequency domain representation is non-zero at locations of the form $f_n = f_0 + n\delta f$.[40]

C. Phase-independent implementation of the Mølmer–Sørensen gate

The phase-sensitive configuration of the two-ion Mølmer–Sørensen gate, as used in the Honeywell device, is discussed by Lee et al.[41] The gate produces the transitions

$$
\begin{aligned}
|gg\rangle &\to \frac{1}{\sqrt{2}}\left(|gg\rangle - ie^{i(\phi_1+\phi_2)}|ee\rangle\right), \\
|ge\rangle &\to \frac{1}{\sqrt{2}}\left(|ge\rangle - i|eg\rangle\right), \\
|eg\rangle &\to \frac{1}{\sqrt{2}}\left(|eg\rangle - i|ge\rangle\right), \\
|ee\rangle &\to \frac{1}{\sqrt{2}}\left(|ee\rangle - ie^{-i(\phi_1+\phi_2)}|gg\rangle\right),
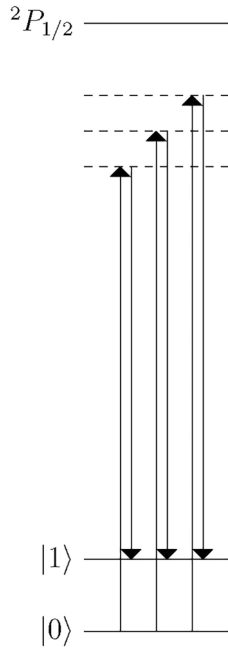\end{aligned}
\tag{2}
$$

FIG. 18. The interaction of opposing optical combs with an ion. In this example, the three shown frequency differences between the teeth of the combs implement stimulated Raman transitions, as shown in Fig. 8, with $E_\Delta = |n_d\rangle - |n_d - 1\rangle$ to induce a Mølmer–Sørenson XX-gate.

with respective spin phases

$$\phi_i = -\frac{1}{2}(\Delta k_{red}X_i - \Delta\phi_{red} + \Delta k_{blue}X_i - \Delta\phi_{blue}),$$

of the ions, based on the wave vector and phase differences $\Delta k_{red/blue}, \Delta\phi_{red/blue}$ of the two red and two blue detuned beams of light driving the stimulated Raman transitions, and X_i as the equilibrium position of the ith ion, using axial motional coupling. The dependency is eliminated from the phase-dependent implementation by rotating the SQs with SQ gates, before and after implementing the TQ gate, with copropagating light sources.

Figure 19 illustrates the counteraction with the phase-dependent implementation. Here, for $\phi = \phi_1 + \phi_2$, SQs $U_{SQ}(\phi) = \exp\left(-i\frac{\pi}{4}(X\cos\phi + Y\sin\phi)\right)$ conjugate the two-ion gate $U_{MS}(\phi) = \exp\left(-i\frac{\pi}{4}(X\sin\phi + Y\cos\phi)^{\otimes 2}\right)$ in order to remove the phase dependence, resulting in the unitary transformation $U_{ZZ} = \exp\left(-i\frac{\pi}{4}Z \otimes Z\right)$. Together with the arbitrary SQs, this gate then generates a universal gate set.

While none of these calculations account for the Ba ions, the CM calculations hold constant for Yb–Ba–Ba–Yb and Ba–Yb–Yb–Ba. The ions have their symmetry maintained during the application of the gate. As the lasers will be detuned from the Ba sidebands, there will be little to no coupling with the Ba internal states.

IX. ERROR MEASUREMENT

Dynamic Rabi pulses to periodically rotate the qubit and correct for long-lasting asymmetric fields are a standard method of decoupling the computer from its environment. In the Honeywell computer, oppositely phased pulse pairs of a global microwave field are applied
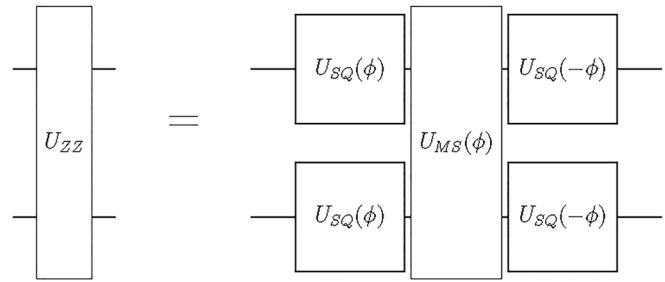

FIG. 19. The gate used in the Honeywell computer to resolve phase difficulties in the design of the Mølmer–Sørenson gate. On the left is the resultant quantum gate, U_{ZZ}, which is formed by the conjugation of the original Mølmer–Sørenson gate by SQ gates. This removes the phase dependence and allows the operation of the gate based purely on the Rabi frequency.

during ground-state cooling for the general suppression of memory errors through dynamical decoupling.[42] This effectively eliminates any biased error in qubit manipulation, leaving an unbiased error that increases in variance over time.

For an m-dimensional quantum system, quantum process tomography may provide a theoretical characterization, measuring output density matrices from each of m^2 pure state inputs. However, it tends to downplay errors incurred in-state preparation and measurement. Furthermore, it does not scale well as the dimension m grows in size. A less comprehensive but more practical characterization is offered by the technique of randomized benchmarking, as discussed in Sec. IX B below. The technique relies on sampling from a suitable finite set of unitary matrices.

A. Pauli groups and Clifford groups

The group of unitary matrices consisting of all finite products of the Pauli matrices $\sigma_x, \sigma_y, \sigma_z$ is the (complex form of the) Pauli group $\mathcal{P}_1$. The complex linear span of the Pauli group is the full set of all unitary 2×2-matrices. For a positive integer n, the (complex form of the) Pauli group $\mathcal{P}_m$ is the mth tensor power $\mathcal{P}_1^{\otimes m}$. Take the group $B_m = (\mathbb{Z}/_2)^m$ of classical bit strings $\mathbf{b} = b_1...b_k...b_m$ of length m under componentwise **xor** as a vector space over $\mathbb{Z}/_2$. Identify B_m with the computational basis of $\mathbf{C}^{2^m}$. Then, the (classical) phase space is $B^m \times B^m$ with elements in canonical coordinates $(\mathbf{q}, \mathbf{p})$ and symplectic form $\Omega((\mathbf{q}, \mathbf{p}), (\mathbf{q}', \mathbf{p}')) = \mathbf{p} \cdot \mathbf{q}' + \mathbf{p}' \cdot \mathbf{q} \in \mathbb{Z}/_2$.

The center $\mathfrak{z}$ of $\mathcal{P}_m$ is $\{i^j = \exp(ij\pi/2)|j \in \mathbb{Z}/_4\}$. The inner automorphism group $\mathcal{P}_m/\mathfrak{z}$ of $\mathcal{P}_m$ is the classical phase space. Thus, $\mathcal{P}_m$ is a finite subgroup of the unitary group $U(2^m)$ of order 2^{2m+2}. Each element of $\mathcal{P}_m$ may be written uniquely in the form $i^j X(\mathbf{q})Z(\mathbf{p})$ with bit flips $X(\mathbf{q})|\mathbf{b}\rangle = |\mathbf{q} + \mathbf{b}\rangle$, phase flips $Z(\mathbf{p})|\mathbf{b}\rangle = (-1)^{\mathbf{b} \cdot \mathbf{p}}|\mathbf{b}\rangle$, and $j \in \mathbb{Z}/_4$. Then $[i^j X(\mathbf{q})Z(\mathbf{p}), i^{j'} X(\mathbf{q}')Z(\mathbf{p}')] = (-1)^{\Omega((\mathbf{q},\mathbf{p}),(\mathbf{q}',\mathbf{p}'))}$, so the commutator subgroup $[\mathcal{P}_m, \mathcal{P}_m]$ is $\{\pm 1\}$.[43]

The real form $\mathcal{P}_1^{\mathbb{R}}$ of $\mathcal{P}_1$ is the group of orthogonal matrices consisting of all finite products of the matrices $X = \sigma_x, Z = \sigma_z$, and $Y = i\sigma_y = ZX$. Abstractly, it is the symmetry group D_4 of the square. Each 2×2 unitary matrix U may be written as a complex linear combination $U = c_0 I + c_1 X + c_2 Y + c_3 Z$. The real form $\mathcal{P}_m^{\mathbb{R}}$ of the Pauli group $\mathcal{P}_m$ is the mth tensor power $(\mathcal{P}_1^{\mathbb{R}})^{\otimes m}$. Thus, $\mathcal{P}_m^{\mathbb{R}}$ is a finite subgroup of the orthogonal group $O(2^m)$ of order 2^{2m+1}. In some references, this real form is also described as a Pauli group.

The real form $\mathcal{C}_n^{\mathbb{R}}$ of the Clifford group $\mathcal{C}_n$ is the normalizer

$$N_{\mathrm{O}(2^m)}(\mathcal{C}_m^{\mathbb{R}}) = \{U \in \mathrm{O}(2^m) | U\mathcal{P}_m^{\mathbb{R}}U^\dagger = \mathcal{P}_m^{\mathbb{R}}\}$$

in $\mathrm{O}(2^m)$ of the subgroup $\mathcal{P}_m^{\mathbb{R}}$. It is finite of order $2^{m^2+m+2}(2^m-1)$ $\prod_{j=1}^m (4^j - 1)$, only including the global phases ± 1. The Clifford group $\mathcal{C}_m$ itself is defined to be the set of all those matrices in $N_{\mathrm{U}(2^m)}(\mathcal{C}_m)$ whose entries are complex numbers of the form $a + b\exp(i\pi/2)$ with rational numbers a, b. It is finite of order $2^{m^2+2m+3}\prod_{j=1}^m (4^j - 1)$. Along with the elements of $\mathcal{P}_m$, it includes Hadamard gates $I_2 \otimes \ldots \otimes H_2 \otimes \ldots \otimes I_2$, CNOT-gates, and, for any $\mathbb{Z}/4$-valued quadratic form $\zeta(\mathbf{b})$ on B, local phase changes $|\mathbf{b}\rangle \to i^{\zeta(\mathbf{b})}|\mathbf{b}\rangle$ on each bit string $\mathbf{b}$.[43]

The Clifford group $\mathcal{C}_m$ forms a three-design, in the sense that the statistical process of selecting random elements from $\mathcal{C}_m$ has mean, variance, and skewness that agree with sampling from $\mathrm{U}(2^m)$ according to its Haar measure.[44] By the Gottesman–Knill theorem, Clifford gates may be simulated efficiently on classical computers while affording universal quantum computation when combined with ancilla states and measurements.[45]

B. Randomized benchmarking

A simple test involving qubit initialization, gate runs, and readout is deceptive: it measures the error rate of the entire process. Of more interest is how a quantum computer scales with deeper circuits, where readout and initialization errors become increasingly insignificant. The technique of randomized benchmarking uses a random computation with a simple model for qubit error. It separates gate and transport errors, which occur at each computation step, from initialization and readout errors, which do not.

Randomized benchmarking of m-dimensional quantum systems selects a random depth-d sequence $U_1, \ldots, U_d$ of unitary matrices from the Clifford group $\mathcal{C}_m$ and adds a final unitary matrix U_{d+1} such that $U_{d+1}U_d\ldots U_1 = I$.[46,47] The Clifford gates act on an initially prepared state $|\psi\rangle$ with state matrix ρ_ψ, and at the end, the positive operator valued measure (POVM) element E_ψ is applied as a measurement. In an errorless run of the gates in the sequence, $\rho_\psi = |\psi\rangle\langle\psi| = E_\psi$. Individual gate errors are modeled by operators $\Lambda_1, \ldots, \Lambda_{d+1}$, so the particular run behavior with these errors is modeled by the sequence operator $\mathcal{S}(\rho) = S\rho S^\dagger$ with $S = \Lambda_{d+i}U_{d+i}\Lambda_d U_d\ldots\Lambda_1 U_1$, yielding a fidelity or survival probability of $\mathrm{Tr}(E_\psi \mathcal{S}(\rho_\psi))$.[48]

In practice, repeated runs are made to yield an average fidelity $F_{d,\psi}$. For general error accounting, it is reasonable to assume gate-independent and time-independent errors Λ_j. Fitting to the fidelity model $F_{d,\psi} = Ap^m + B$ yields a probability $\alpha = p$ and average error rate $r = (1-p) - (1-p)/m$. The constants A and B handle errors in-state preparation, the concluding gate U_{d+1}, and the final measurement.

1. Honeywell benchmarking

The Honeywell literature provides figures showing the survival rates $1 - p$. For SQ gates, orders of $1 - p = 10^{-3}$ are attained, and $1 - p = 10^{-2}$ for TQ gates, with fidelity around 3×10^{-3} for state preparation and readout.

2. IonQ benchmarking

IonQ measured SQ gates in a configuration with 11 qubits.[3] Over 500 tests of $\pi/2$ gates in sequences of length $2, 4, \ldots, 12$, the error rate was found to be 3×10^{-3}. A state preparation and measurement (SPAM) rate of 5×10^{-3} was observed. This is the quantity $A + B$, corresponding to measuring an ion after a single π rotation.

For TQ gates, a slightly modified approach was taken. A single XX-gate application was used to prepare two qubits in the Bell state $\frac{1}{\sqrt{2}}(|00\rangle + e^{i\phi}|11\rangle)$. The probabilities of the qubits being in the respective $|0\rangle$ and $|1\rangle$ states on readout are taken as P_{ij} for $i, j = 0, 1$. Measuring the Bell state directly is insufficient to determine whether the qubits are entangled, due to the possibility of a mixed state. To resolve this, after creation of the Bell state, a parity oscillation consisting of a $\pi/2$ pulse with phase ϕ is applied to each qubit. The final state is expected to have probabilities $\Phi = P_{00} + P_{11} - P_{01} - P_{10}$. The fidelity was measured as $F = \frac{1}{2}(P_{00} + P_{11} + \Phi)$. An approximate error rate between 1.1×10^{-2} and 4.9×10^{-2} was observed.

C. Quantum volume

The Honeywell device is claimed to exhibit the largest quantum volume, 64, of any contemporary quantum computer (at the time of writing). Thus, we will briefly discuss the concept of quantum volume, as presented computationally in Ref. 49 on the basis of the related theoretical definition in Ref. 50. Roughly, the quantum volume (which might more appropriately be called a "quantum area") tracks the largest product of depth d and width m for a random circuit that will successfully run on the given device. The computational version proceeds from the premise that quantum supremacy is reflected in the classical complexity of simulating the probability distribution of outputs from a quantum circuit, dealing with the heavy output generation problem.[51]

Consider a circuit of depth d, involving m qubits, defined by a unitary operator U. Possible outputs $\mathbf{b}$ are bit strings of length m taken from the $\mathbb{Z}/2$-space B_m with zero $\mathbf{0} = 0^m$; the computation is initialized with $|\mathbf{0}\rangle$. The classical probability distribution of the outputs is given by $p_U(\mathbf{b}) = |\langle \mathbf{b}|U|\mathbf{0}\rangle|^2$. An output $\mathbf{b}$ is said to be heavy if $p_U(\mathbf{b})$ is above the median of the distribution p_U. In an ideal device, where this distribution would be exponential, the proportion of heavy outputs is $(1 + \log 2)/2 \simeq 0.85$.[51] At the other extreme, in a completely depolarized device, just half of the outputs would be heavy.

In the computational approach of Ref. 49, the heavy output generation problem for an actual computer requires its native gates to produce circuits U for which the proportion of heavy outputs exceeds $2/3$, to within a desired statistical significance. Such circuits are deemed to have achieved success. For each value of m that is feasible on the machine, successful circuits U of depth $d = m$ are sought. If M is the maximum value of m leading to success on a given machine, then the quantum volume of that machine is defined to be 2^M.

X. CONCLUSION

We have summarized contemporary ion transport and control, qubit configuration, gate implementation, and error characterization in ytterbium ion trap quantum computer practice. Many further optimizations can occur with more precise TQ application, faster cooling, faster ion transport, improved trap design, and more complex ion addressal methods.

Differing approaches to error analysis complicate comparisons across different computational schemes. The Honeywell quantum computer is, at the time of this review, the most complete, and despite IonQ's potential to scale faster, cross-talk error may become significant as a result of its architecture.

Many alternative designs are possible, which allow scaling if contemporary techniques reach their limit. The use of ytterbium is not limited to Yb–Yb TQ gates. Experiments on Yb–Ba linking via motional coupling have been performed, suggesting the possibility for more advanced quantum coupling with multiple ion types. Modularity can, in theory, be achieved by using photonic coupling between ionic computers at a low error rate, which would fit well with the illumination and detection procedures of contemporary architectures.

More complex arrangements may be expected to achieve significant improvement. Physical systems are usually constrained to use the simplest configurations possible to reduce engineering errors in the final product. However, the use of ytterbium ions in quantum computation provides an example of a complex, stable system in nature, allowing for the benefits of sustained improvement without the drawbacks of worrying that the electronic eigenstates could vary. Cross-talk minimization opens the possibility that contemporary computational designs might be scalable in line with the quantum threshold theorem.[52] The techniques that we have discussed are competitive at the time of writing, but are certainly open to future development.

ACKNOWLEDGMENTS

AUTHOR DECLARATIONS
Conflict of Interest

The authors have no conflicts to disclose.

DATA AVAILABILITY

The data that support the findings of this study are available upon reasonable request from the corresponding author.

APPENDIX: BARIUM

Some of the use cases of barium in the Honeywell design had significant overlap with our treatment of ytterbium. We give a brief overview of the technical details here.

For even Ba^+ ions, there is no hyperfine structure. Zeeman splitting does occur and is imposed on the ions. This corroborates the need for a magnetic field to quantize the qubit.[23]

A fast scheme for the selection of $^{138}Ba^+$ requires that a source of barium be heated and then illuminated by a trichroic scheme. A 791 nm laser resonant to the $6s^2\,^1S_0 \leftrightarrow 6s6p\,^3P_1$ transition is used with another laser set to either 310 or 337 nm. This is sufficient for photoionization, but not fast. For electron repumping, a laser set to 650 nm is tuned to the $5D_{3/2} \leftrightarrow 6P_{1/2}$ transition. This repumps electrons, which decay from $6s6p\,^3P_1$ to $5D_{3/2}$, ionizing the Ba. Doppler cooling is likewise performed as discussed in Sec. IV A 1.[53]
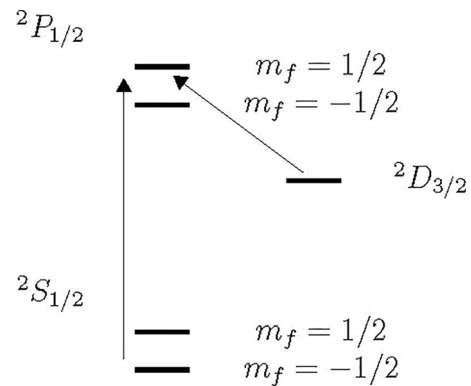

FIG. 20. $^{138}Ba^+$ Doppler cooling. Broadening allows indiscriminate transitions between Zeeman levels. States are prevented from being trapped in the $^2D_{3/2}$ structure by the secondary stimulated transition (as described in Ref. 23).

1. Doppler cooling

For Doppler pumping, as in Fig. 20, the beam is taken at 493.5 nm with no detuning. This is applied for 20 ms. No data are available for what the average motional state $\bar{n}$ is after Doppler cooling. Optionally, a wide linewidth beam resonant to the $^2P_{1/2} \leftrightarrow {}^2D_{3/2}$ transition is used to pump electrons from the metastable $^2D_{3/2}$ level. The Honeywell paper reports times on the order of 10 ms for the resulting cooling time. However, this is not particularly worrisome, as Doppler cooling takes place before the computation is started and so does not affect the performance of the quantum computer's fidelity or runtime.

REFERENCES

[1]J. Cirac and P. Zoller, Phys. Rev. Lett. **74**, 4091 (1995).
[2]P. Goldner, A. Ferrier, and O. Guillot-Noël, "Chapter 267: Rare earth-doped crystals for quantum information," in *Handbook on the Physics and Chemistry of Rare Earths* (Elsevier, New York, 2015), Vol. 46, p. 1.
[3]K. Wright *et al.*, Nat. Commun. **10**, 5464 (2019).
[4]D. Kielpinski, C. Monroe, and D. Wineland, Nature **417**, 709 (2002).
[5]C. Monroe, R. Raussendorf, A. Ruthven, K. Brown, P. Maunz, L. Duan, and J. Kim, Phys. Rev. A **89**, 022317 (2014).
[6]C. Monroe, D. Meekhof, B. King, W. Itano, and D. Wineland, Phys. Rev. Lett. **75**, 4714 (1995).
[7]J. Pino *et al.*, Nature **592**, 209–213 (2021).
[8]S. Olmschenk, K. Younge, D. Moehring, D. Matsukevich, P. Maunz, and C. Monroe, Phys. Rev. A **76**, 052314 (2007).
[9]S. Debnath, N. Linke, C. Figgatt, K. Landsman, K. Wright, and C. Monroe, Nature **536**, 63–66 (2016).
[10]U. Tanaka, K. Suzuki, Y. Ibaraki, and S. Urabe, J. Phys. B **47**, 035301 (2014).
[11]D. Berkeland, J. Miller, J. Bergquist, W. Itano, and D. Wineland, J. Appl. Phys. **83**, 5025 (1998).
[12]D. Stick, K. Fortier, R. Haltli, C. Highstrete, D. Moehring, C. Tigges, and M. Blain, arXiv:1008.0990 (2010).
[13]J. Home, D. Hanneke, J. Jost, D. Liebfried, and D. Wineland, New J. Phys. **13**, 073026 (2011).
[14]G. Pagano *et al.*, Quantum Sci. Technol. **4**, 014004 (2019).
[15]P. Maunz, *High Optical Access Trap 2.0.* (Sandia National Laboratory, Albuquerque, 2016).
[16]T. Hänsch and A. Schawlow, Opt. Commun. **13**, 68 (1975).
[17]D. Wineland, C. Monroe, W. Itano, D. Leibfried, B. King, and D. Meekhof, J. Res. Natl. Inst. Stand. Technol. **103**, 259 (1998).
[18]S. An, J. Zhang, M. Um, D. Lv, Y. Lu, J. Zhang, Z. Yin, H. Quan, and K. Kim, Nat Phys. **11**, 193 (2015).

[19] U. Tanaka, T. Kitanaka, K. Hayasaka, and S. Urabe, Appl. Phys. B **121**, 147 (2015).

[20] J. Chen, K. Wright, N. Pisenti, D. Murphy, K. Beck, K. Landsman, J. Amini, and Y. Nam, Phys. Rev. A **102**, 043110 (2020).

[21] M. Barrett et al., Phys. Rev. A **68**, 042302 (2003).

[22] C. Monroe, D. Meekhof, B. King, S. Jefferts, W. Itano, D. Wineland, and P. Gould, Phys. Rev. Lett. **75**, 4011 (1995).

[23] C. Seck, M. Kokish, M. Dietrich, and B. Odom, Phys. Rev. A **93**, 053415 (2016).

[24] M. Acton, K. Brickman, P. Haljan, P. Lee, L. Deslauriers, and C. Monroe, Quantum Inf. Comput. **6**, 465 (2006).

[25] D. Berkeland and M. Boshier, Phys. Rev. A **65**, 033413 (2002).

[26] R. Noek, G. Vrijsen, D. Gaultney, E. Mount, T. Kim, P. Maunz, and J. Kim, Opt. Lett. **38**, 04735 (2013).

[27] Y. Xie, X. Zhang, B. Ou, T. Chen, J. Zhang, C. Wu, W. Wu, and P. Chen, Phys. Rev. A **95**, 032341 (2017).

[28] M. House, Phys. Rev. A **78**, 033402 (2008).

[29] H. Lau and D. James, Phys. Rev. A **83**, 062330 (2011).

[30] M. Palmero, R. Bowler, J. Gaebler, D. Leibfried, and J. Muga, Phys. Rev. A **90**, 053408 (2014).

[31] R. Bowler, J. Gaebler, Y. Lin, T. Tan, D. Hanneke, J. Jost, J. Home, D. Leibfried, and D. Wineland, Phys. Rev. Lett **109**, 080502 (2012).

[32] D. Allcock et al., App. Phys. B **107**, 913 (2012).

[33] F. Splatt, M. Harlander, M. Brownnutt, F. Zähringer, R. Blatt, and W. Hänsel, New J. Phys. **11**, 103008 (2009).

[34] A. Sørensen and K. Mølmer, Phys. Rev. Lett. **82**, 1971 (1999).

[35] G. Milburn, arXiv:quant-ph/9908037 (1999).

[36] A. Sørensen and K. Mølmer, Phys. Rev. A **62**, 022311 (2000).

[37] N. Grzesiak et al., Nat. Commun. **11**, 2963 (2020).

[38] S. Zhu, C. Monroe, and L. Duan, Phys. Rev. Lett. **97**, 050505 (2006).

[39] C. Figgatt et al., Nature **572**, 368–372 (2019).

[40] D. Hayes et al., Phys. Rev. Lett. **104**, 140501 (2010).

[41] P. J. Lee et al. J. Opt. B: Quantum Semiclass. Opt. **7**, S371 (2005).

[42] L. Viola, E. Knill, and S. Lloyd, Phys. Rev. Lett. **82**, 2417 (1999).

[43] A. Calderbank, E. Rains, P. Shor, and N. Sloane, IEEE Trans. Inf. Theory **44**, 1369 (1998).

[44] Z. Webb, Quantum Inf. Comput. **16**, 1379 (2016).

[45] S. Aaronson and D. Gottesman, Phys. Rev. A **70**, 052328 (2004).

[46] J. Gambetta et al., Phys. Rev. Lett. **109**, 240504 (2012).

[47] C. Baldwin, B. Bjork, D. Gaebler, D. Hayes, and D. Stack, Phys. Rev. Res. **2**, 013317 (2020).

[48] E. Magesan, J. Gambetta, and J. Emerson, Phys. Rev. Lett. **106**, 180504 (2011).

[49] A. Cross, L. Bishop, S. Sheldon, P. Nation, and J. Gambetta, Phys. Rev. A **100**, 032328 (2019).

[50] N. Moll et al., Quantum Sci. Technol. **3**, 030503 (2018).

[51] S. Aaronson and L. Chen, arXiv:1612.05903 (2017).

[52] R. Rausendorf and J. Harrington, Phys. Rev. Lett. **98**, 190504 (2007).

[53] B. Wang, J. Zhang, C. Gao, and L. Wang, Opt. Express **19**, 16438 (2011).